Nanoscale

PAPER

View Article Online
View Journal

Cite this: DOI: 10.1039/d5nr04118j

Charge transport and trap state engineering in transition metal-doped bismuth vanadate photoanodes: a DFT study

Balaji G. Ghule,[a] Seung Gyu Gyeong[a] and Ji-Hyun Jang *[a,b]

Bismuth vanadate ($BiVO_4$, BVO) is a widely studied photoanode material for photoelectrochemical (PEC) water splitting due to its suitable band gap, which enables efficient visible light absorption. However, its practical performance is significantly limited by poor charge carrier separation and low mobility, resulting in high recombination rates and reduced photocatalytic efficiency. To overcome these challenges, we propose a novel doping strategy involving the substitution of V^{5+} sites with cations of varying oxidation states, specifically 4^+, 5^+, and 6^+ to modulate the structural, electronic, and catalytic properties of BVO. Using density functional theory (DFT) calculations, we systematically investigate the impact of these dopants on the crystal structure, electronic band structure, charge transport behavior, and oxygen evolution reaction (OER) energetics. Among the doped systems, Ti^{4+}-doped BVO (Ti-BVO) demonstrates superior OER performance, primarily due to a reduced hole effective mass and an improved charge carrier mobility of 0.3802 $cm^2\ V^{-1}\ s^{-1}$ for holes and 0.1527 $cm^2\ V^{-1}\ s^{-1}$ for electrons. Additionally, the increased diffusion lengths for holes (99.2 nm) and electrons (62.89 nm) contribute to more efficient charge separation and transport. The calculated overpotential for Ti-BVO is significantly reduced to 0.41 V, compared to 0.97 V for pristine BVO, indicating a substantial improvement in reaction kinetics. These findings provide valuable insights for designing BVO-based next-generation photoanode materials.

Received 29th September 2025,
Accepted 16th January 2026

DOI: 10.1039/d5nr04118j

rsc.li/nanoscale

1. Introduction

Bismuth vanadate (BVO) is a highly promising photocatalyst for solar energy conversion, owing to its nontoxicity, affordability, photostability, and eco-friendly characteristics.[1,2] Among its three crystalline polymorphs, monoclinic clinobisvanite (m-BVO) exhibits the highest photocatalytic activity, attributed to its optimal band gap of 2.4–2.9 eV.[3–6] However, recent studies have identified limitations in m-BVO due to the low mobility of photogenerated charge carriers (electron–hole pairs), a positive conduction band potential (*vs.* NHE), and high charge recombination rates, significantly hindering its practical applications. Enhancement in the photocatalytic activity of m-BVO can be achieved through approaches such as metal or non-metal doping, heterojunction formation with other semiconductors, deposition of cocatalysts, defect engineering (*e.g.*, oxygen vacancies), crystal facet optimization, and morphological modifications.[7–9] While many studies have explored doping BVO at vanadium (V) or bismuth (Bi) sites and oxygen (O) sites,[10] previous research has extensively examined doping at V sites,[11–18] which, although common, often leads to distortions in the $[VO_4]$ tetrahedral chains due to varying valence states of the dopants. Such distortions can cause a phase transition from the monoclinic to tetragonal structure, adversely affecting photocatalytic water-splitting and hydrogen generation.

Recent studies show that doping with 4^+, 5^+, and 6^+ valence state dopants can maintain the structure of the $[VO_4]$ tetrahedral chains in *m*-BVO and potentially increase its water splitting performance.[19–21] Also, attempts have been made to engineer the various crystal facets of BVO to enhance its water splitting activity. In a theoretical study reported by Lardhi *et al.*, the DFT results predict the BVO (001) facet as the only good candidate for both the HER and the OER, while the (010) facet is a suitable candidate for the OER only. The (110) and (121) surfaces are acceptable candidates only for the OER but have less potential than the (001) and (010) surfaces.[22]

In contrast to the experimental investigation, theoretical analysis by computer simulation is expected to clarify in detail the metal doping effects. In recent years, density functional theory (DFT) calculations have made important contributions to solving this issue. Recently, Li *et al.* explored halogen atom doping (Cl, Br, and I) in BVO to enhance its electronic pro-

[a]*School of Energy and Chemical Engineering, Department of Energy Engineering, Graduate School of Carbon Neutrality, Graduate School of Semiconductor Materials and Devices Engineering, Ulsan National Institute of Science and Technology, Ulsan-44919, Republic of Korea. E-mail: clau@unist.ac.kr*
[b]*Department of Chemical Engineering, Faculty of Engineering, Chulalongkorn University, Bangkok 10330, Thailand*

perties for solar water splitting applications. Research shows that doping at oxygen sites under oxygen-poor conditions is energetically favorable, even at higher concentrations. Halogen doping modifies BVO's energy levels, enhances redox capability, and suppresses photoexcited carrier recombination. These effects intensify with increased dopant concentration, especially with iodine. Overall, the study confirms that halogen doping is a promising strategy to improve the photocatalytic performance of BVO-based photoanodes.[23] Massaro *et al.* conducted a first-principles DFT + U study to investigate the effects of Mo and W doping on the photocatalytic performance of BVO. Mo-doping notably reduces the OER overpotential to 0.68 V by stabilizing the high-energy *O intermediate, aligning with experimental evidence of improved n-type conductivity. In contrast, W-doping does not lower the overpotential due to the high energy required for *OOH formation, though it still improves hydration.[24]

Previous theoretical work has typically focused on single transition metal dopants or specific properties in isolation. To the best of our knowledge, there have been limited theoretical investigations into the origin of transition metal doping effects on BVO. Crucially, several fundamental questions remain unanswered: (1) How does the local chemical environment of different dopants systematically impact the electronic structure and charge transport behavior? (2) What is the quantitative influence of a wide range of dopants on catalytic activity relevant to solar water splitting (OER energetics)?

To address these gaps, in the present work, we systematically examine the structural and electronic properties, charge transport, and OER energetics of BVO doped with transition metals (Ti^{4+}, Zr^{4+}, Hf^{4+}, Nb^{5+}, Ta^{5+}, Cr^{6+}, Mo^{6+}, and W^{6+}) using first-principles calculations. From the previously reported experimental[25,26] and theoretical works,[27] the substitution of dopants replacing the V site is more favorable or thermodynamically stable compared to the Bi site. Therefore, the optimized structure of pristine BVO was used for cation doping, where a V^{5+} atom is replaced by a dopant metal atom. Both bulk and (001) faceted BVO systems are considered to provide a comprehensive understanding of doping effects. A direct comparison of the influence of different dopants is presented, and the relationship between structural features and catalytic activity is discussed. This work also offers insights that may guide future experimental efforts in optimizing BVO-based OER catalysts.

2. Computational methods

Theoretical calculations analyzing the effect of transition metal doping on structural, electronic, and charge transport properties of BVO were carried out using spin-polarized density functional theory (DFT), implemented *via* the Vienna *Ab initio* Simulation Package (VASP).[28] The Perdew–Burke–Ernzerhof (PBE) functional was employed within the generalized gradient approximation (GGA)[29] to account for exchange–correlation effects. The projector augmented wave (PAW) method[30] was used to describe the ion–electron interactions, with spin polarization included. The electronic wavefunctions were expanded using a plane-wave energy cutoff of 400 eV.[22] Structural relaxations were performed with an energy convergence criterion of 1×10^{-5} eV, and the maximum force threshold was set to 0.01 eV $Å^{-1}$. A Monkhorst–Pack *k*-point mesh of $2 \times 2 \times 3$ was used for Brillouin zone sampling of the $1 \times 1 \times 1$ unit cell. The electronic density of states and band structure of pure and doped BVO were evaluated using the HSE06 hybrid functional to find better agreement with the experimental data.[31,32] Additional details regarding the charge transport characteristics and OER energetics calculations are available in the SI.

3. Results and discussion

3.1. Crystal and electronic structure

To analyse the effect of cation doping on the crystal and electronic structure of BVO, we initially optimized the pristine BVO and then doped transition metals by replacing the V atom for each dopant. The side and top views of the conventional pristine clinobisvanite BVO structure are shown in Fig. 1(a). Pristine clinobisvanite BVO crystallizes in a monoclinic structure (space group *I*2/*b*), where Bi^{3+} ions are coordinated by oxygen in a distorted 8-fold polyhedron and V^{5+} ions form slightly distorted VO_4 tetrahedra.[33] These tetrahedra are linked *via* shared oxygen atoms, forming a 3D network that stabilizes the monoclinic lattice. The structure exhibits anisotropic bonding, which influences its electronic and optical properties. The optimized structure of pristine BVO was used for cation doping, where a V^{5+} atom is replaced by the dopant metal atom, as shown in Fig. 1(b). The optimized structural parameters of pristine and transition metal-doped bulk BVO, including lattice constants (*a*, *b*, and *c*), the monoclinic β angle, the unit cell volume, and the resulting strain induced by doping, are shown in Table 1. The pristine BVO exhibits lattice parameters of a = 7.251 Å, b = 11.582 Å, and c = 5.125 Å with a β angle of 134.974°, which is consistent with the experimental results,[34,35] yielding a unit cell volume of 304.554 $Å^3$.

Upon doping with various cations, noticeable variations in the lattice parameters and unit cell volume are observed, indicating that the substitution of V with dopants of different ionic radii induces lattice distortions. For instance, Ti^{4+} doping slightly reduces the lattice constants and results in a negative strain (−1.2%), suggesting a compressive effect due to the smaller ionic radius of Ti^{4+} (0.66 Å) compared to that of V^{5+} (0.52 Å).[36] Conversely, doping with larger cations such as Nb^{5+}, Ta^{5+}, and W^{6+} causes an expansion of the lattice, as reflected by increased unit cell volumes (up to 307.647 $Å^3$ for W-BVO) and positive strain values (1%).

The strain values in the table quantify these lattice modifications, with values ranging from −1.2% (Ti-BVO) to 1% (W-BVO). The degree of strain introduced is crucial, as it can influence the electronic structure and charge transport properties of the material. Overall, this table highlights how cation doping modulates the crystal structure of BVO, which in turn can affect its photoelectrochemical performance.

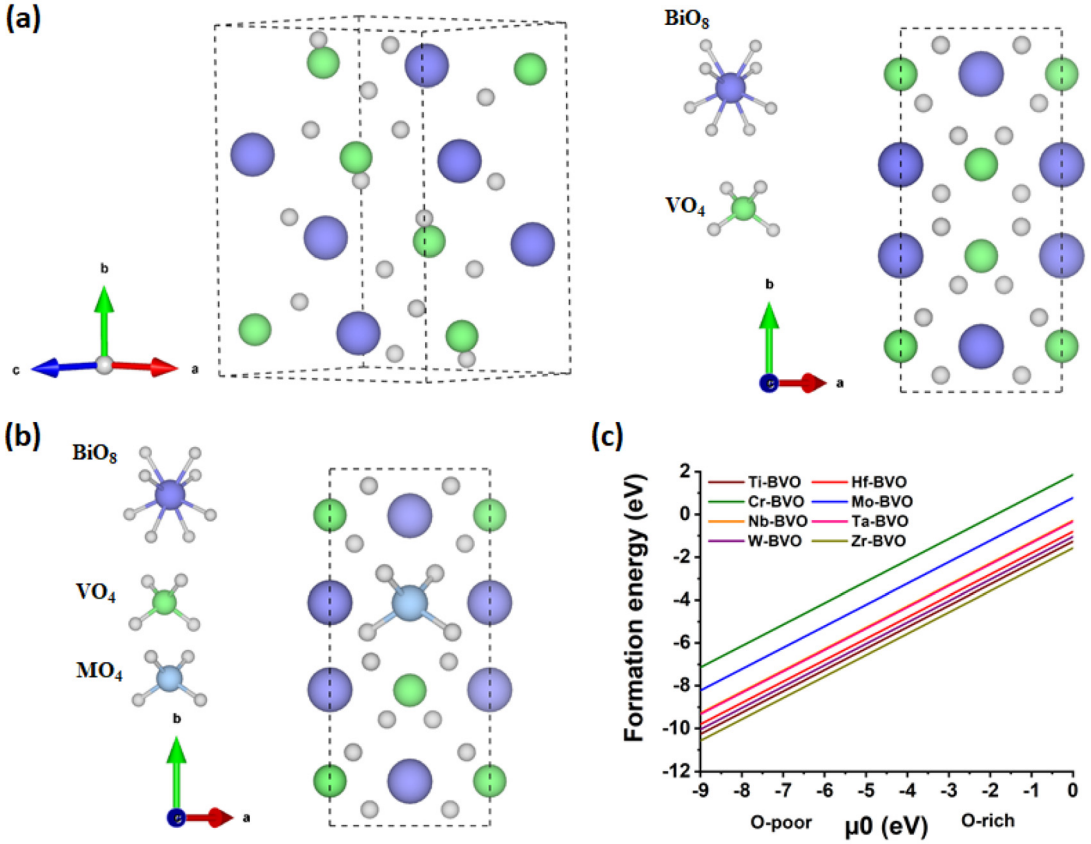

Fig. 1 (a) Side and top views of the conventional unit cell of pristine BVO, (b) top view of metal-doped BVO, and (c) calculated formation energies of metal-doped BVO. The blue, green, grey and sky-blue balls represent Bi, V, O, and dopant atoms, respectively.

Table 1 Optimized structural parameters of pure and doped BVO

Photoanode	a (Å)	b (Å)	c (Å)	β (°)	Cell volume (Å^3)	Strain (%)
BVO	7.251	11.582	5.125	134.974	304.554	0.00
Ti-BVO	7.242	11.467	5.120	134.950	300.950	−1.20
Zr-BVO	7.298	11.42	5.155	134.844	304.737	0.06
Hf-BVO	7.253	11.438	5.113	134.201	304.19	−0.01
Nb-BVO	7.303	11.508	5.161	135.030	306.593	0.06
Ta-BVO	7.309	11.503	5.165	135.04	306.876	0.07
Cr-BVO	7.224	11.574	5.107	135.031	301.829	−0.09
Mo-BVO	7.295	11.522	5.155	134.998	306.44	0.06
W-BVO	7.314	11.516	5.167	135.032	307.647	1.00

The synthetic feasibility and solubility limits of dopants in $BiVO_4$ are largely determined by the dopant's ionic radius and oxidation state matching with those of the host V^{5+} ion and the associated formation energy of necessary charge-compensating defects. Low oxidation state dopants like Ti^{4+}, Hf^{4+}, and Zr^{4+} are easily soluble in $BiVO_4$ due to lower charge imbalance while substituting V^{5+}. Iso-valent dopants like Nb^{5+} and Ta^{5+} have high solubility due to minimal lattice disruption and charge imbalance.

However, aliovalent (different valence) dopants, such as the high-valence Cr^{6+}, Mo^{6+}, and W^{6+}, require charge compensation mechanisms, typically the formation of oxygen/cation vacancies and reduction of V^{5+} adjacent to doping sites to V^{4+}. The dopants like Mo^{6+} and W^{6+} are well studied and show good experimental solubility (up to ~10 at%).[7] The synthesis of Cr^{6+}-doped $BiVO_4$ is generally more problematic, with lower solubility limits caused by increased lattice strain and the formation of potentially detrimental, complex defects that limit performance. Our theoretical predictions correlate well with these known experimental trends, highlighting a lower theoretical formation energy for the functional dopants with a concentration of 4.17 at%.

Therefore, we analyze the dopant formation energy (E_f), which is a widely accepted method, to compare the relative

degree of solubility in the host materials for different metal dopants incorporated into the lattice of BVO. Among the considered metal dopants for BVO, Ti^{4+} exhibits the lowest formation energy, indicating that it can be more easily incorporated into the host lattice during synthesis.[37,38] The low formation energy reflects the thermodynamic ease with which Ti^{4+} can substitute V^{5+}, meaning that less energy is required to form the doped structure. This makes Ti^{4+} a highly soluble dopant in BVO, capable of achieving higher equilibrium concentrations without forming secondary phases. Hf^{4+}- and Zr^{4+}-doped BVO have higher formation energies than Ti^{4+} due to their larger ionic radii, *i.e.*, 0.78 Å for Hf^{4+} and 0.79 Å for Zr^{4+}, compared to Ti^{4+} (0.66 Å).[39]

In contrast, Cr shows the highest formation energy, largely because Cr^{6+} has a higher oxidation state and a smaller ionic radius (0.44 Å), and the need for charge compensation mechanisms, such as oxygen/cation vacancies, and reduction of V^{5+} to V^{4+}. These factors make Cr less thermodynamically favorable and reduce its solubility in BVO. Nb and Ta, both pentavalent and similar in size to V^{5+}, exhibit nearly identical formation energies, suggesting comparable substitution behavior and solubility. W^{6+} shows lower formation energy than Cr^{6+} in BVO due to favorable electronic interactions, *i.e.*, W^{6+}'s 5d orbitals enable strong overlap with O 2p orbitals, forming stable W–O bonds that reduce the energy cost of substitution, and lower tendency to destabilize the host lattice, making it a more effective and soluble dopant for enhancing the photoelectrochemical performance.

3.2. Effect of doping on the electronic structure

The effect of transition metal doping on the electronic structure of BVO is shown in Fig. 2 and Fig. S1. The evaluated electronic band structures and total density of states (TDOS) for pristine and transition metal-doped BVO systems, specifically Ti^{4+}, Nb^{5+}, and Mo^{6+} dopants, calculated using the HSE06 hybrid functional, are shown in Fig. 2. The electronic band structures and TDOSs for Zr^{4+}-, Hf^{4+}-, Ta^{5+}-, Cr^{6+}- and W^{6+}-doped BVO systems are shown in Fig. S1.

In Fig. 2(a) and Fig. S1(a), pristine BVO exhibits an indirect band gap of 2.64 eV, in agreement with the experimental findings.[3] The relatively flat valence and conduction bands suggest low intrinsic carrier mobility, especially for holes. The corresponding DOS shows a symmetric distribution around the band gap without any mid-gap states, indicating a clean semiconducting nature with limited defect states. Fig. S2(a) shows the projected band structure of pristine BVO consisting of mostly O 2p states in the VBM and V 3d states dominating the conduction band.

Ti^{4+} doping in BVO (Fig. 2(b)) leads to a notable reduction in the band gap to 2.25 eV, which can be attributed to the introduction of Ti^{4+} states that hybridize with the CB, effectively lowering its edge. The increased dispersion of the conduction band indicates a reduced effective mass of electrons, thereby enhancing their mobility. This is corroborated by the TDOS, which shows a higher density near the CBM, suggesting improved charge carrier transport and a potential boost in the photocatalytic efficiency.

The projected band structure (Fig. S2(b)) confirms the presence of shallow trap states just above the VBM and near the Fermi level. These shallow trap states are likely due to the substitutional incorporation of Ti^{4+} into the BVO lattice, which introduces localized states that facilitate charge separation without significantly increasing recombination losses.[40]

Fig. S1(b) and (c) show the band structures and TDOSs of Zr^{4+}- and Hf^{4+}-doped BVO, respectively. In these cases, the band gaps are slightly reduced to 2.45 eV for Zr-BVO and 2.5 eV for Hf-BVO. The modest reduction suggests weaker interaction between the dopant orbitals and the host conduction band compared to Ti^{4+} doping. Additionally, both Zr^{4+} and Hf^{4+} doping introduces deeper trap states above the VBM (as confirmed in Fig. S3(c)), which may act as recombination centers, potentially limiting charge carrier lifetimes.[41]

Fig. S2(b) and (c) further reveal that Hf^{4+} doping results in the deepest trap states among the three dopants, indicating stronger localization of electronic states. This could hinder charge transport more significantly than Ti^{4+} doping, thereby affecting photocatalytic performance. Deep trap states (from Zr^{4+} and Hf^{4+}) tend to trap holes. Hole trapping reduces the number of mobile holes that can reach the surface and participate in the OER, so these are usually detrimental to OER kinetics and efficiency.

Doping BVO with Nb^{5+} (Fig. 2(c)) results in a modest band gap reduction to 2.49 eV. This slight narrowing can be attributed to the introduction of Nb 4d states, which interact weakly with the conduction band edge, thereby lowering its energy. Although the overall band dispersion remains similar to that of pristine BVO, the increased electronic states near the CBM suggest enhanced electron availability, indicative of n-type semiconducting behavior.[42] This could facilitate improved electron conduction, beneficial for photocatalytic and photoelectrochemical applications.

Similarly, Ta^{5+} doping (Fig. S1(d)) leads to a slightly greater band gap reduction to 2.35 eV. This effect is likely due to the stronger contribution of Ta 5d orbitals near the CBM, which increases the number of electronic states and further lowers the conduction band edge. The enhanced CBM states may improve charge carrier separation and transport, contributing positively to the photocatalytic performance.[43]

Projected band structures shown in Fig. S2(d) and (e) confirm that neither Nb^{5+} nor Ta^{5+} doping introduces mid-gap trap states between the valence band maximum (VBM) and the CBM. The absence of deep or shallow trap states implies that the band gap reduction is intrinsic to the dopant-induced band edge modulation, rather than the defect-related states. Consequently, these dopants maintain the electronic integrity of the BVO lattice while subtly tuning its optical and transport properties.

In the case of Mo-doped BVO (Fig. 2d), the band gap is further reduced to 2.25 eV. The DOS shows high densities near both the CBM and the VBM, which could improve both light absorption and charge separation efficiency. A shallow trap

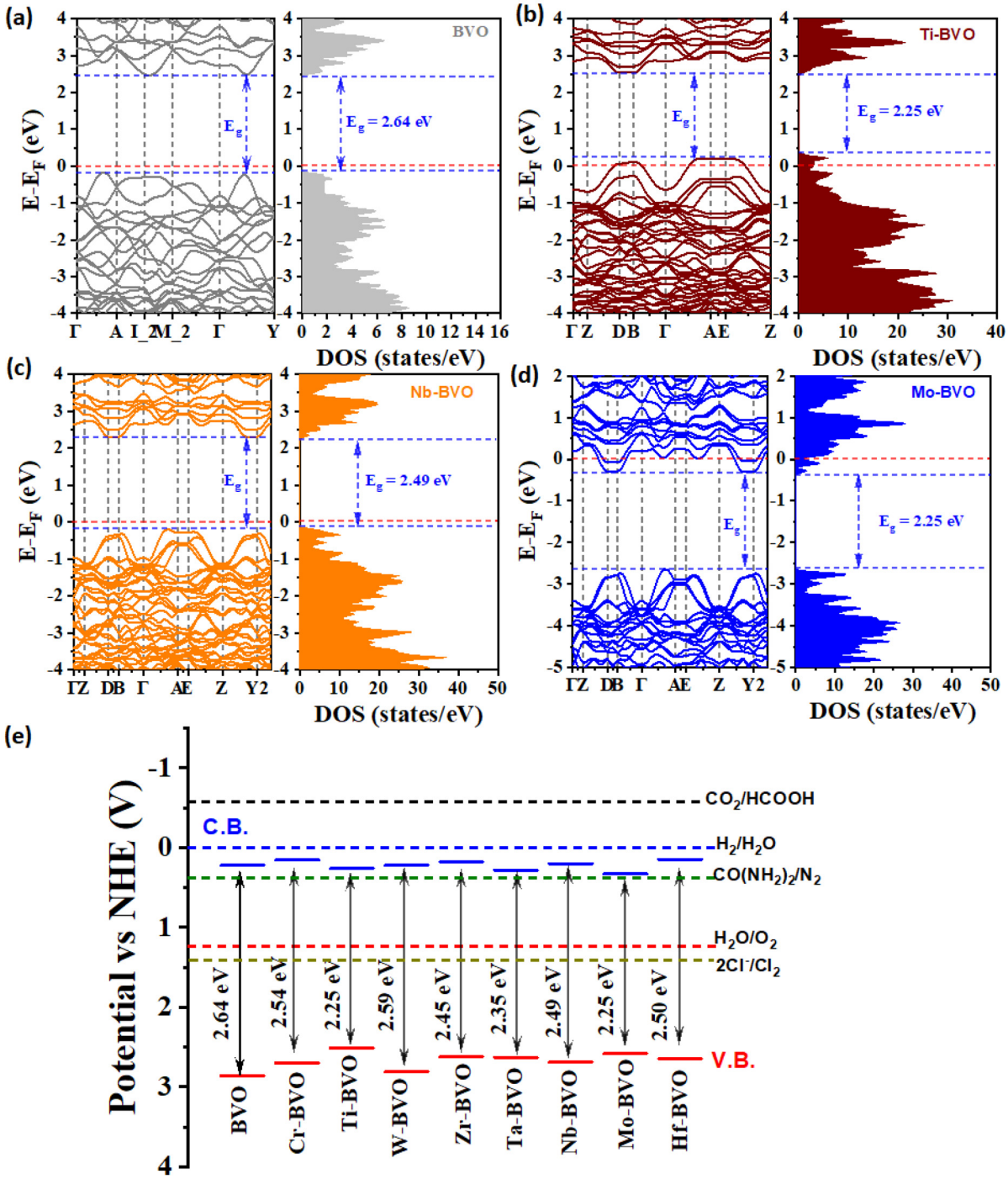

Fig. 2 DFT-calculated electronic band structures and total DOSs of (a) pure; (b) Ti^{4+}-doped, (c) Nb^{5+}-doped, and (d) Mo^{6+}-doped bulk BVO, respectively, and (e) calculated band gaps and band edge positions of pure and doped bulk BVO using the HSE06 method. The VB and CB values are given concerning the standard redox potentials *vs.* NHE for water splitting.

state near the CBM is observed, which is attributed to the incorporation Mo^{6+}, which is further confirmed by the 2D charge density maps in Fig. 4(d) and Fig. S2(h). The shallow trap state near the CBM can be beneficial for electron trapping and increasing the recombination time.[37] Fig. S1(e) and (f) show the band structure and TDOS of Cr^{6+}- and W^{6+}-doped BVO, where a mild reduction in the band gap is observed. However, W^{6+} introduces very shallow trap states near the conduction band, which can enhance electron mobility but may also lead to insufficient charge separation. These overly shallow states allow electrons to quickly recombine with holes, which is corroborated by the 2D charge density maps in

Fig. S3(d), thereby hindering the OER process. In contrast, Cr^{6+} creates deeper trap states near the conduction band that can localize electrons (as shown in Fig. S3(c)) and act as recombination centers, ultimately hindering OER efficiency.[44]

Fig. 2e shows a comparison of the calculated band edge positions (CBM and VBM) of pristine and TM-doped BVO with respect to the normal hydrogen electrode (NHE). The redox potentials for water splitting are marked at 0 V (H^+/H_2) and 1.23 V (H_2O/O_2). For efficient photoelectrochemical (PEC) water splitting, the CBM must lie above 0 V to facilitate proton reduction and the VBM must lie below 1.23 V to drive oxygen evolution. All the investigated doped systems satisfy these criteria, indicating their thermodynamic viability for overall water splitting. Notably, the Ti- and Mo-doped BVO samples retain favorable band alignments while also exhibiting reduced band gaps, making them particularly promising for visible-light-driven PEC applications. In addition, some dopants such as Cr, W, and Ta also show slight upward shifts in the VBM, which could aid hole transport and improve OER kinetics. The calculated band gaps for pure and doped $BiVO_4$ using the standard HSE06 parameters are approximately in the range of 2.64–2.25 eV, respectively, which is in excellent agreement with the experimentally reported values.[45–51]

3.3. Effect of doping on the charge transport

Fig. 3 provides a comprehensive comparison of effective masses, carrier mobilities, and diffusion lengths for the pristine and transition metal-doped bulk BVO photoanodes, the key parameters that govern photoelectrochemical performance, particularly for the oxygen evolution reaction (OER). In pristine BVO, the relatively large effective masses of electrons ($1.892m_e$) and holes ($0.915m_e$) suggest restricted carrier transport, which has been a major bottleneck in achieving high-efficiency water oxidation with the BVO-based photoanodes.

Upon doping with transition metals such as Ti, Zr, Hf, Nb, Ta, Cr, Mo, and W, a general reduction in both electron and hole effective masses is observed. Among these, Ti-doped BVO exhibits the lowest effective masses ($1.15m_e$ for electrons and $0.462m_e$ for holes), suggesting significantly improved charge transport behavior.

The doping environment changes the electronic band structures and thus affects the carrier effective masses. We observed

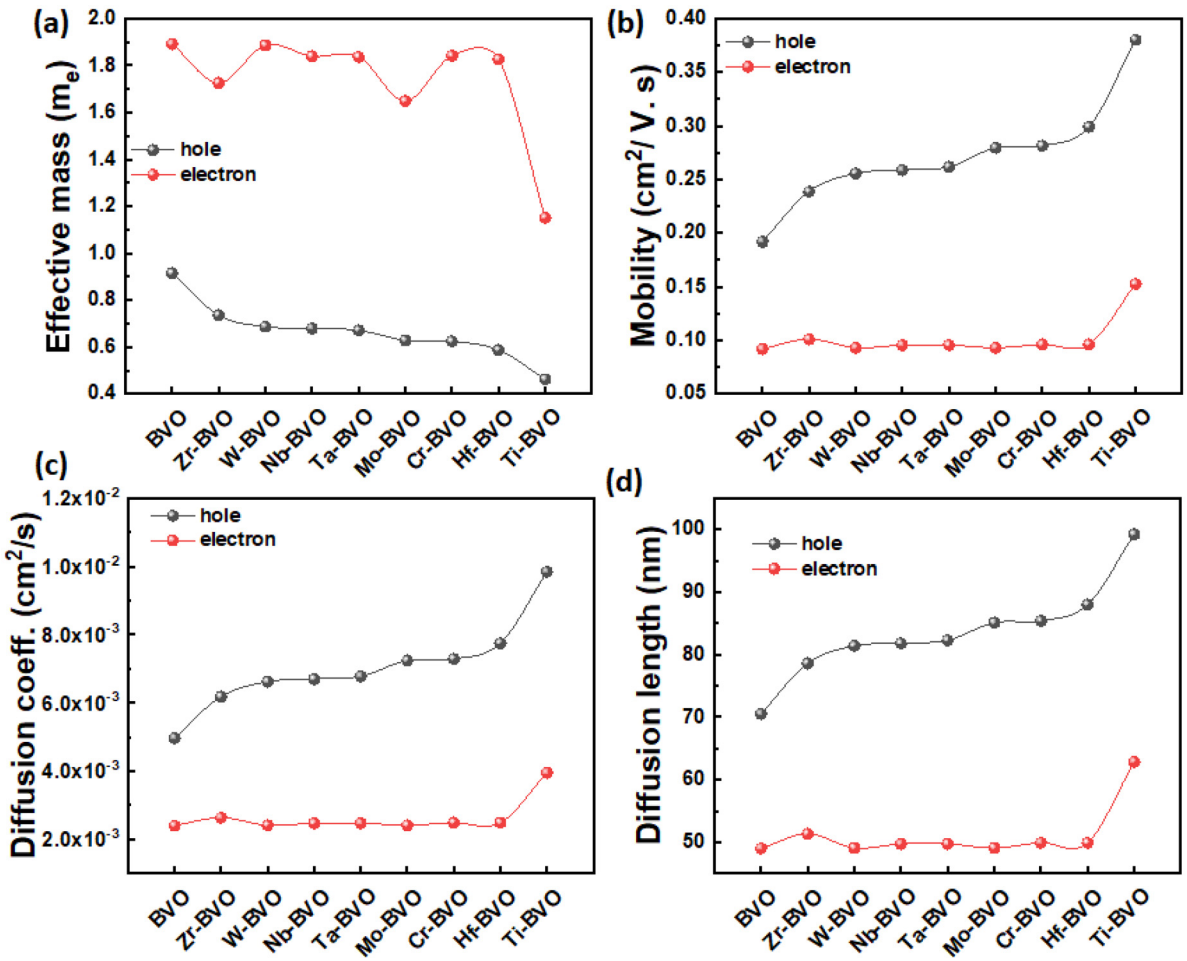

Fig. 3 Calculated (a) electron and hole effective masses, (b) carrier mobilities, (c) diffusion lengths, and (d) charge carrier diffusion coefficients for pristine and doped BVO, highlighting the impact of doping on charge transport properties.

that the dopants with smaller ionic radii like Cr (0.44 Å) can cause the lattice distortion and flatten the curvature of the electronic band structure corresponding to a larger effective mass, whereas dopants like Ti^{4+} (0.66 Å), Nb^{5+} (0.64 Å), Ta^{5+} (0.64 Å), Mo^{6+} (0.60 Å), and W^{6+} (0.60 Å) with ionic radii similar to that of the host atom V^{5+} (0.52 Å) have shown more stable structures and smaller effective masses.

The dopants with larger ionic radii like Zr^{4+} (0.72 Å) and Hf^{4+} (0.71 Å) have shown the larger effective masses compared to the other dopants, owing to the structural distortion and the flattened electronic band structure.

It is known that the lower electronegativity typically lowers the effective mass and *vice versa*, the same trend we have observed in our study. The dopants like Zr^{4+} (0.72 Å) and Hf^{4+} (0.71 Å) with larger ionic radii and smaller electronegativities (Zr^{4+} (1.4) and Hf^{4+} (1.3)) have shown larger effective masses in this study. Therefore, we consider that the ionic radius is more significant for the effective mass reduction.

This reduction in effective masses directly translates to increased carrier mobilities, where Ti-BVO shows the highest values of 0.1527 $cm^2\ V^{-1}\ s^{-1}$ for electrons and 0.3802 $cm^2\ V^{-1}\ s^{-1}$ for holes, more than doubling the hole mobility compared to pristine BVO. Notable enhancements in hole mobility are also observed with dopants including Cr, Hf, and Zr. This improvement is crucial because hole transport currently represents the rate-limiting step in the OER process. A comparison of carrier mobility obtained in this study with previous reports is shown in Table S2.

The diffusion coefficients of both pristine and doped BVO were evaluated using eqn (4), as detailed in the SI. For pristine BVO, the electron diffusion coefficient was found to be $2.4 \times 10^{-7}\ m^2\ s^{-1}$. Out of all the dopants explored, Ti-doped BVO exhibited the highest diffusion coefficients for both charge carriers, with values of $9.84 \times 10^{-7}\ m^2\ s^{-1}$ for holes and $3.95 \times 10^{-7}\ m^2\ s^{-1}$ for electrons. This enhancement in carrier diffusion is likely responsible for the improvement in the charge transfer efficiency of Ti-doped BVO.[52]

A carrier's average travel distance before recombination is known as the diffusion length and is a crucial determinant of OER activity. Pristine BVO exhibits a hole diffusion length of 70.5 nm, which is near the minimum effective threshold. Ti^{4+} doping extends this length to 99.2 nm, ensuring a greater proportion of photogenerated holes migrate to the surface sites. The Cr^{6+}- and Hf^{4+}-doped BVO samples also show improved lengths (85.4 nm and 88.0 nm), enhancing the probability of efficient water oxidation at the semiconductor–electrolyte boundary.

Transition metal doping, particularly using Ti^{4+}, boosts the performance of BVO photoanodes by improving how charge carriers move and reducing energy loss. These changes increase surface hole accumulation and enhance the OER activity, showing that dopant engineering is a key strategy for improving the solar water splitting efficiency.

3.4. Charge density difference analysis

The obtained results in Fig. 4 and Fig. S3 show the charge density difference and 2D-charge density maps for the pure and doped BVO systems. These visualizations provide critical insights into how cation doping alters the electronic environment and charge distribution within the bulk BVO lattice.

The first thing to notice in Fig. 4(a) is how symmetrical the pristine BVO charge distribution is, reflecting its natural, stable bonding structure. The 2D map clearly illustrates strong Bi–O interactions through distinct red (accumulation) and blue (depletion) lobes.

Fig. 4(b) shows the charge redistribution caused by Ti^{4+} doping. Notable changes occur around the Ti site and adjacent oxygen atoms, primarily an increase in charge accumulation that indicates enhanced orbital hybridization between Ti and O. This increased electron density is predicted to improve both electronic conductivity and charge separation, which is highly beneficial for photoelectrochemical performance.[53] Conversely, the Hf^{4+}-doped system (Fig. S3a) exhibits a less significant charge distribution change. The 2D map confirms reduced interaction and less distributed charge density around the Hf and O atoms when compared directly to the Ti^{4+} doping results.

In the case of Nb^{5+} doping (Fig. 4c), the charge density difference reveals more delocalized electron accumulation around the Nb site, paired with notable charge depletion from adjacent O atoms. This indicates that Nb functions as an electron donor, modifying the local electronic structure and potentially enhancing the material's n-type behavior. The 2D map confirms this finding with a dispersed charge density distribution that could facilitate enhanced electron mobility. A comparable trend is observed for Ta^{5+} doping (Fig. S3b), where the electron concentration and charge accumulation are also increased around the Ta atom, and the 2D map illustrates the resulting interaction and charge redistribution between the Ta and O atoms.

Fig. 4(d) shows that Mo^{6+} doping causes major charge redistribution. We observe intense charge accumulation near Mo and moderate depletion in surrounding O atoms, indicating a robust interaction and effective charge transfer. The 2D charge density map visually confirms this with a widespread, intense concentration of charge around the Mo atom, suggesting an enhanced electronic coupling that is key for improving how carriers (electrons) are transported through the material.

In summary, Fig. 4 highlights how transition metal doping modifies the internal charge distribution of BVO. These changes directly impact the material's electronic properties, such as conductivity and carrier separation efficiency, which are crucial for applications in photoelectrochemical water splitting. The stronger charge redistribution observed in the Ti^{4+}-, Nb^{5+}-, Ta^{5+}- and Mo^{6+}-doped systems, in particular, suggests their potential for boosting the performance of BVO.

3.5. Oxygen evolution reaction (OER)

The free energy diagrams of the pristine and doped BVO samples are shown in Fig. 5 and Fig. S4. The free energy diagrams for the pristine BVO and Ti^{4+}-doped, Nb^{5+}-doped, and Mo^{6+}-doped BVO (001) surfaces are shown in Fig. 5. The green line represents the ideal catalyst energies for each intermediate

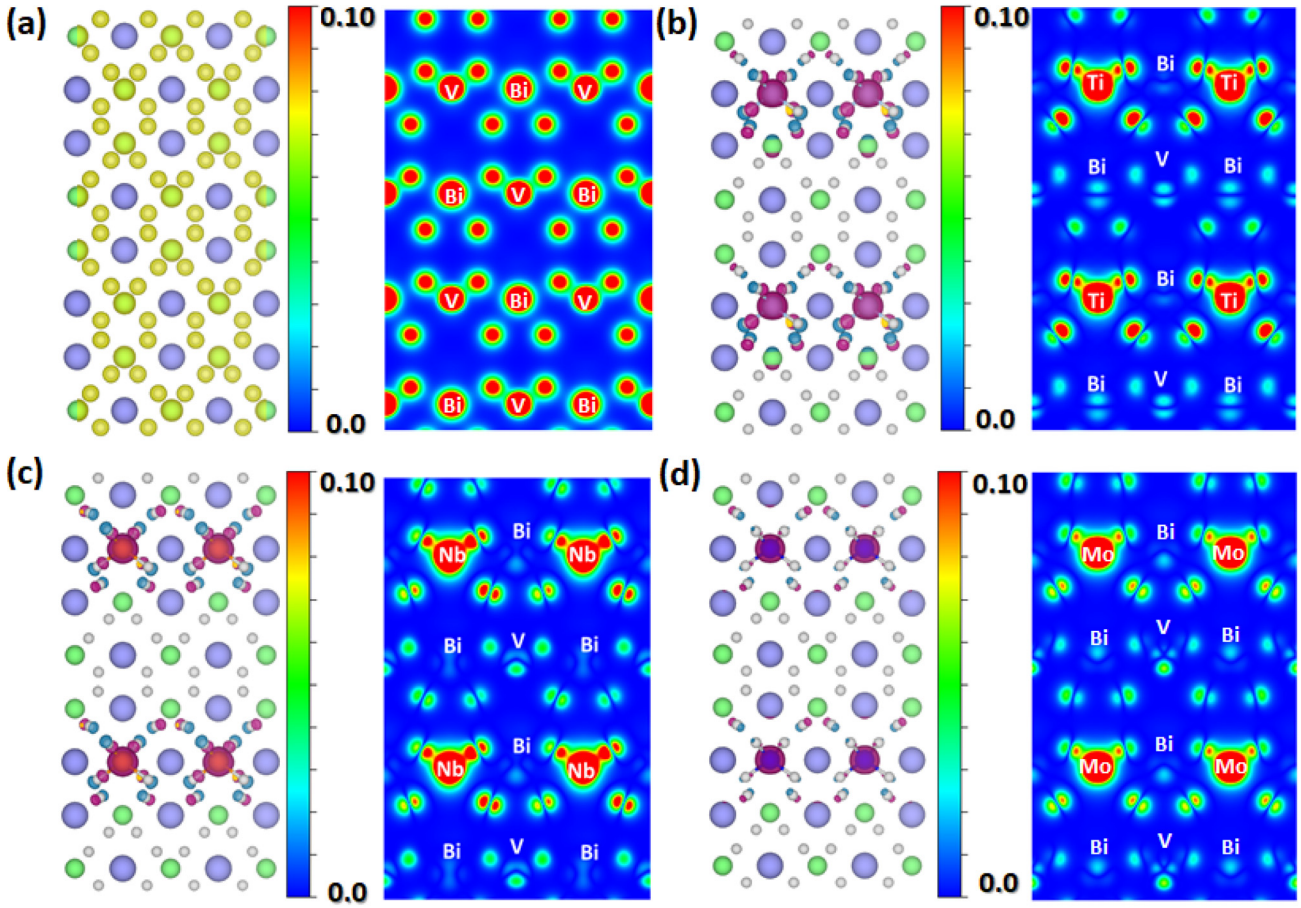

Fig. 4 DFT-calculated charge density difference and 2D-charge density maps of the (001) plane for (a) pure bulk BVO; (b) Ti^{4+} cation-doped, (c) Nb^{5+} cation-doped, and (d) Mo^{6+} cation-doped bulk BVO, respectively. The iso-surface value was set to 0.05 eV $Å^{-3}$. The dark-cyan and purple color regions represent the charge accumulation and depletion, respectively. The red and light-green regions in the 2D-charge density map represent the higher and lower charge regions, respectively.

step in the OER pathway. The black line shows the calculated free energies at 0 V, the red line corresponds to the free energies at an applied potential of 1.23 V, and the blue line illustrates the free energies after accounting for the potential-determining step (PDS). Pristine BVO (Fig. 5(a) and Fig. S4(a)) shows the second intermediate step, *i.e.*, OH* → O*, as the potential determining step (PDS) for water oxidation with a potential of 2.20 V. The PDS gives an overpotential of 0.97 V for the pristine BVO, *i.e.*, when an external potential of 1.23 V is applied, and the second intermediate step has an energy barrier of 0.97 V.

Pristine BVO exhibits the highest charge transfer (−0.62*e*) and strongest adsorption (−1.19 eV); such strong binding can hinder the desorption of intermediates, limiting turnover in multistep reactions like the OER.[54]

From Fig. 5(b) and Fig. S4(b), it can be seen that Ti-BVO shows the most effective OER performance and overpotential (0.41 V) with a PDS of 1.64 V for the second intermediate step, *i.e.*, OH* → O*, in the four-electron step process. The obtained overpotential in this study is much lower compared to the previously reported experimental overpotentials of 0.44 eV[55] and 0.97 V.[56] This improvement correlates with the DFT-calculated charge density difference (CDD) plots and charge transferred (Fig. 6(b)), which show moderate charge transfer (−0.50*e*) and the lowest OH adsorption energy (−0.29 eV), indicating optimal binding strength and enhanced reaction kinetics.[57] In contrast, as shown in Fig. 5(c), the PDS of Nb-BVO is shifted to the fourth intermediate step, *i.e.*, OOH* → O_2, with a higher potential (1.98 V), resulting in a higher overpotential (0.75 V) for water oxidation. The corresponding charge transfer (−0.23*e*) and adsorption energy (−0.67 eV) suggest moderately strong OH binding, which still supports catalytic activity but is weaker than Ti-BVO. Fig. S4(c) and (d) present the free energy profiles for the Zr- and Hf-doped BVO samples, respectively. In both doped systems, the PDS, the step that requires the highest energy input and thus controls the overall reaction rate, occurs at the second intermediate of the OER pathway. The energy barriers for this step are 2.09 eV for Zr-BVO and 2.06 eV for Hf-BVO, which correspond to overpotentials of 0.86 V and 0.73 V, respectively, when an external potential of 1.23 V is applied. These overpotentials reflect the extra energy required beyond the thermodynamic minimum to drive the reaction efficiently.

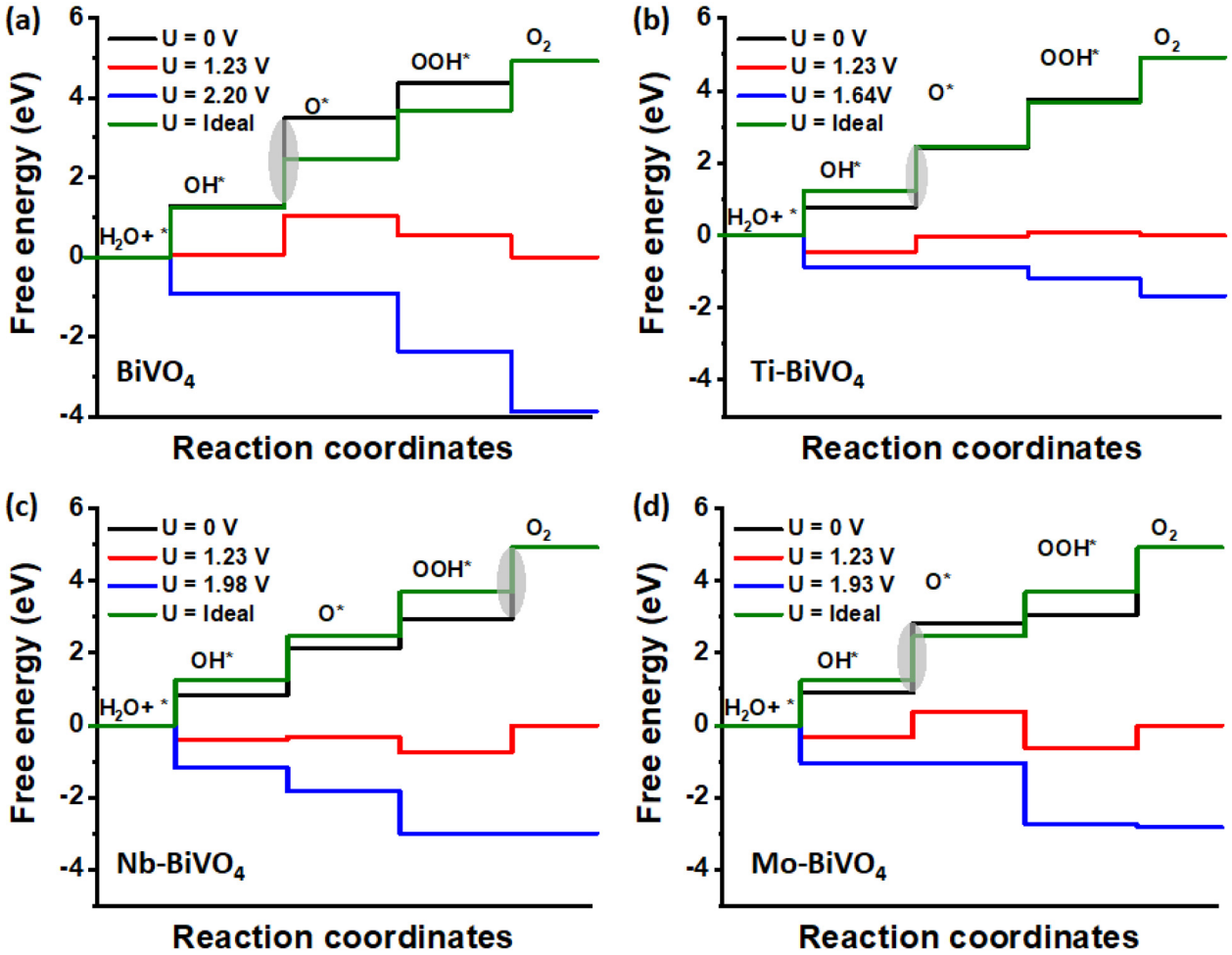

Fig. 5 DFT-calculated Gibbs free energies at different operating potentials for (a) pure BVO; (b) Ti^{4+}-doped, (c) Nb^{5+} cation-doped, and (d) Mo^{6+} cation-doped BVO (001) surfaces.

The charge transfer values (−0.55*e* for Zr-BVO and 0.38*e* for Hf-BVO) and adsorption energies (−0.88 eV for Zr-BVO and 0.90 eV for Hf-BVO) indicate that OH* intermediates bind moderately strongly to the surface. This level of binding is generally favorable, as it supports catalytic activity without overly stabilizing the intermediates, which could hinder their transformation or desorption.[58]

The superior performance associated with Ti^{4+} doping is linked to enhanced orbital hybridization, which can be visualized and confirmed through Projected Density of States (PDOS) analysis, as shown in Fig. S6(a) in the SI. When Ti^{4+} is introduced, it integrates well into the lattice due to its similar size and d-electron character. The PDOS plots show significant energetic overlap between the newly introduced Ti 3d orbitals and the neighboring O 2p orbitals. Unlike Ti^{4+} doping, which introduces states close to the conduction band edge, the hybridization of Hf 3d (Fig. S6(b)) and Zr 4d (Fig. S6(c)) orbitals occurs at much higher energy levels (>5 eV). This indicates that the Hf^{4+} and Zr^{4+} states are less effective at modifying the active band edge regions crucial for visible light absorption and charge transport. A comparison of OER overpotentials obtained in this study with previous reports is shown in Table S2.

Fig. S4(e) shows the energy profile for Ta-doped BVO. Ta-BVO also exhibits moderate OER performance, with a PDS energy barrier of 1.98 eV at the second intermediate, resulting in an overpotential of 0.75 V. The associated charge transfer (−0.48*e*) and adsorption energy (−0.77 eV) again suggest moderately strong OH* binding. This behavior supports catalytic activity comparable to that of Nb-doped systems, although slightly less effective than Ti doping.

In the case of Mo-doped BVO, as shown in Fig. 5(d) and Fig. S4(h), the second intermediate remains the PDS, with a slightly lower overpotential of 0.70 V, despite a relatively high energy barrier of 1.93 eV. The charge transfer (−0.55*e*) and adsorption energy (−0.78 eV) suggest a balanced OH* binding strength, which is beneficial for maintaining catalytic turnover.

Fig. S4(g) and (i) depict the free energy profiles for Cr- and W-doped BVO. For Cr-BVO, the PDS occurs at the fourth intermediate, with an energy barrier of 2.09 eV, leading to an overpotential of 0.91 V. For W-BVO, the PDS is at the second inter-

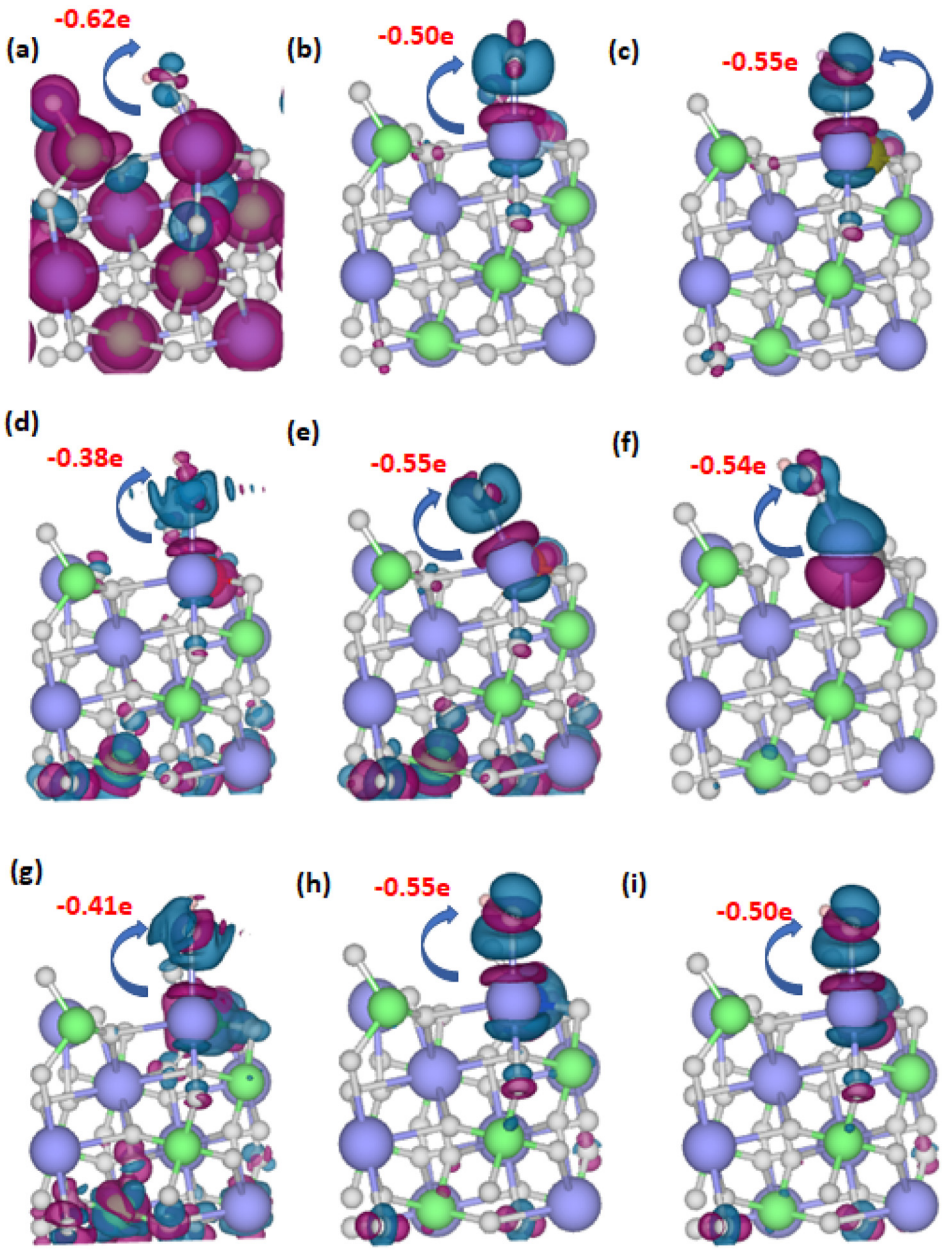

Fig. 6 DFT-calculated charge density difference of OH_{ads} on the (001) surfaces of (a) pure; (b) Ti^{4+}-doped, (c) Zr^{4+}-doped, (d) Hf^{4+}-doped, (e) Nb^{5+}-doped, (f) Ta^{5+}-doped, (g) Cr^{6+}-doped, (h) Mo^{6+}-doped and (i) W^{6+}-doped BVO, respectively. The dark-cyan and purple colors represent the charge accumulation and depletion, respectively. The blue, green, grey, and light-pink balls represent the Bi, V, O, and H atoms, respectively.

mediate, with a barrier of 2.06 eV, corresponding to an overpotential of 0.95 V. The charge transfer to OOH from Cr-BVO is $-0.23e$ and the charge transfer to OH from W-BVO is $-0.33e$. The adsorption energies of 0.19 eV for OOH on Cr-BVO and −0.67 eV for OH on W-BVO suggest moderately strong binding of these intermediates, which is essential for maintaining catalytic efficiency without impeding reaction progression.

Fig. 6 shows the DFT-calculated charge density difference (CDD) plots for OH* adsorption on the (001) surfaces of the various doped BVO systems. In these plots, the dark-cyan iso-surfaces represent regions of charge accumulation, while the purple iso-surfaces indicate charge depletion. These visualizations reveal how electron density redistributes upon OH* adsorption, offering insights into the electronic interactions that govern catalytic behavior. Bader charge analysis, indicated by the sky-blue arrows, quantifies the amount of charge transferred from the surface to the OH* adsorbate.

In the pristine BVO system, the highest charge transfer ($-0.62e$) and strongest adsorption energy (−1.19 eV) are observed. While strong binding can enhance intermediate stabilization, it may also hinder their desorption, thereby lim-

iting the overall reaction turnover, especially in multistep processes like the OER.[59] In contrast, Ti^{4+} doping achieves a more optimal balance, with a moderate charge transfer (−0.50*e*) and the lowest adsorption energy (−0.29 eV) among the studied systems. This correlates with the lowest calculated overpotential, indicating that Ti^{4+} doping effectively tunes the surface reactivity to favor efficient OER kinetics. Overall, Ti^{4+} doping provides the most favorable catalytic profile by optimizing both charge transfer and intermediate binding, followed by Mo^{6+}, Hf^{5+}, Nb^{5+}, Ta^{5+} and Zr^{4+} whereas W^{6+} and Cr^{6+} appear less promising for efficient OER catalysis. OH adsorption bond lengths and bond angles obtained in this study are shown in SI Table S1.

3.6. Effect of doping on the optical properties

The absorption spectra of the pure and doped $BiVO_4$ samples were calculated and are shown in Fig. S7(a). Obviously, pure $BiVO_4$ has intensive adsorption in the visible light region. The adsorption edge of pure $BiVO_4$ is found to be 475 nm, which is comparable to the measured value. For all doped systems, the absorption edges exhibit a red shift (meaning that they absorb longer wavelengths/lower energy light) compared to the pure material (Fig. S7(b)). The magnitude of this red shift follows a specific order: the Hf-doped sample has the largest shift, followed by the Ta-, Zr-, Ti-, W-, Nb-, and Mo-doped systems.

The most substantial red shift observed in the doped BVO system is likely attributed to an electronic transition originating from an impurity level within the band structure to the conduction band.[60] Crucially, every one of the tested doped materials maintains strong light absorption capabilities within the desired visible light spectrum.

Fig. S7(c) shows the calculated real part of the dielectric function for pure and doped BiVO4 across the photon energies. All materials show relatively high, positive values for (ε_1). This indicates strong polarization and a high refractive index in the visible light range (which roughly spans from 1.6 eV to 3.1 eV). At 0 eV (static limit), the (ε_1) values are the highest, representing the static dielectric constant. There is a prominent peak across all materials in this region. This peak is associated with the onset of the fundamental electronic transitions (band gap absorption).

The various dopants (Cr, Hf, Mo, Nb, Ta, Ti, W, and Zr) cause minor shifts and changes in the intensity of the main peaks and general dispersion curves. These subtle changes reflect the modification of the electronic band structure by the different dopant atoms, which introduces new energy levels and alters the available electronic states. The data highlight that these materials are strong dielectrics with significant responses to visible light, making them promising candidates for photocatalytic applications.

Fig. S7(d) shows the imaginary part of the dielectric function (ε_2) for the pure and various doped $BiVO_4$ compounds, plotted against photon energies. The point where the curves begin to rise sharply from zero indicates the band gap energy of the material. For pure BVO (black line), this onset is around 2.0–2.2 eV. Below this energy, the material is transparent to light; above this energy, absorption begins. The visible light spectrum spans roughly from 1.6 eV (red) to 3.1 eV (violet). The figure shows that all these materials exhibit strong absorption within this visible range, consistent with their use as visible-light-active materials.

The addition of dopants like Cr, Hf, Mo, Nb, Ta, Ti, W, and Zr (colored lines) modifies the absorption profile. The primary absorption peaks shift slightly in energy compared to pure BVO, indicating changes in the electronic band structure, often leading to the creation of impurity levels within the band gap. The intensity (height of the ε_2 values) of the absorption also changes, suggesting that some doped materials might absorb more or less efficiently than the pure material at specific energies.

3.7. Mechanism of doping effects on the OER

The OER on BVO is a complex, multi-step process that relies on the efficient generation, separation, and surface transfer of photogenerated holes to oxidize water molecules into oxygen.[61] In its pure form, BVO suffers from poor bulk conductivity and rapid electron–hole recombination, which limits the number of holes reaching the surface to participate in the formation of key intermediates such as OH, O, and OOH.[62–64] These limitations result in sluggish reaction kinetics and low overall photocatalytic efficiency, making doping a critical strategy to enhance the performance (Fig. 7).

Doping with tetravalent (4^+) cations like Ti^{4+}, Zr^{4+}, and Hf^{4+} modifies the electronic structure in distinct ways. Ti^{4+} introduces shallow acceptor states near the valence band, facilitating hole transfer to the surface, which enhances intermediate formation and accelerates the OER.[65] In contrast, Zr^{4+} and Hf^{4+} introduce deep trap states near the valence band that immobilize holes and increase recombination. Hf^{4+} forms deeper traps than Zr^{4+}, making it more detrimental to OER kinetics.[66] Meanwhile, pentavalent (5^+) dopants like Nb^{5+} and Ta^{5+} act as clean donors, increasing the carrier concentration without introducing trap states. This trap-free doping allows for efficient hole transport and sustained catalytic activity, significantly boosting the OER performance.[43,67] When Ta^{5+} or Nb^{5+} ions substitute for V^{5+} in the BVO lattice, they act as donor dopants. This means that they introduce extra electrons into the system without disrupting the charge balance, since they have the same oxidation state as vanadium. These additional electrons contribute to the conduction band, effectively increasing the electron carrier concentration and improving bulk conductivity. This enhancement in conductivity helps in facilitating better charge separation and transport, which is crucial for improving the efficiency of the OER.

Hexavalent (6^+) dopants such as Mo^{6+}, W^{6+}, and Cr^{6+} have varied effects. Mo^{6+} and W^{6+} introduce shallow trap states near the conduction band, which temporarily hold electrons and suppress recombination while maintaining high mobility.[43,68] This enhances charge separation and supports rapid formation of OER intermediates. Cr^{6+}, however, introduces deep trap states near the mid-gap that immobilize holes and

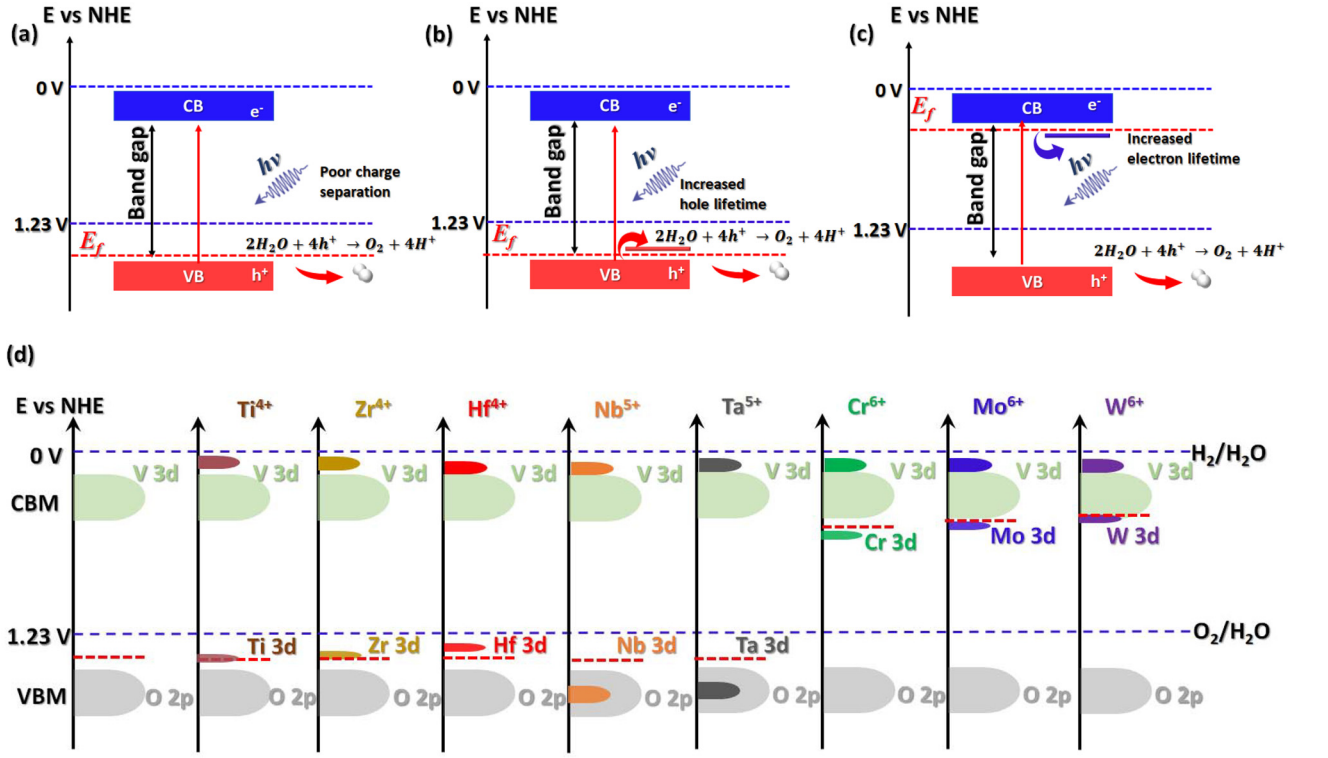

Fig. 7 Mechanism of the doping effects on the OER process. (a) Pristine BVO, (b) 4^+ cation-doped BVO, and (c) 6^+ cation-doped BVO and (d) schematic of bands and trap states redrawn from band structure calculations.

promote recombination, reducing the number of active carriers available for water oxidation. As a result, while Mo^{6+} and W^{6+} improve OER kinetics, Cr^{6+} tends to hinder it unless carefully managed through co-doping or surface modification. Understanding these dopant-specific effects is essential for designing high-performance BVO photoanodes tailored for efficient solar-driven water splitting.

4. Conclusion

In conclusion, doping BVO photoanodes with cations significantly influences their photoelectrochemical OER performance by modifying trap states, carrier dynamics, and reaction energetics. Among tetravalent dopants, Ti^{4+} is the most effective, introducing shallow trap states that enhance charge separation and transport. It also exhibits the highest hole mobility (~0.3802 $cm^2\ V^{-1}{\cdot}s^{-1}$) and the longest hole diffusion length (~100 nm), contributing to superior charge dynamics. Density functional theory (DFT) calculations reveal that Ti-doped BVO has the lowest OER overpotential (0.41 V), indicating highly favorable reaction energetics. Meanwhile, Ta^{5+} and Nb^{5+} do not introduce trap states but significantly enhance the electrical conductivity of BVO, leading to improved OER activity compared to pristine BVO. In comparison, Mo^{6+} introduces shallow trap states near the conduction band that improve electron mobility and bulk conductivity, with a DFT-calculated overpotential of 0.71 V. Although W^{6+} introduces shallow trap states near the conduction band that improve electron mobility, its DFT-evaluated overpotential of ~0.91 V makes it thermodynamically less favorable for the OER. Zr^{4+} offers moderate improvements, while Hf^{4+} and Cr^{6+} introduce deeper trap states that can increase recombination and hinder performance. Overall, Ti^{4+}, Nb^{5+}, Ta^{5+}, and $Mo^{6+}$are the most promising dopants for enhancing BVO photoanode efficiency in solar-driven water splitting applications.

Conflicts of interest

The authors declare that they have no known competing financial interests or personal relationships that could have appeared to influence the work reported in this paper.

Data availability

The authors confirm that all data supporting the findings of this study are available within the article and its supplementary information (SI). Computational methods and additional supporting data, including electronic structure results, charge density difference analyses, and two-dimensional charge density maps, are available in the Supporting Information. See DOI: https://doi.org/10.1039/d5nr04118j.

Acknowledgements

This work was supported by the National Research Foundation of Korea (NRF) grant funded by the Korean government (MSIT) (No. RS-2020-NR049543, RS-2025-16072057,and RS-2025-00553591). The authors are thankful to the UNIST Supercomputing Center for providing the high-performance computation facility.

References

1 M. Tayebi and B. K. Lee, Recent advances in $BiVO_4$ semiconductor materials for hydrogen production using photoelectrochemical water splitting, *Renewable Sustainable Energy Rev.*, 2019, **111**, 332–343.

2 S. Wang, X. Wang, B. Liu, Z. Guo, K. K. Ostrikov, L. Wang and W. Huang, Vacancy defect engineering of $BiVO_4$ photoanodes for photoelectrochemical water splitting, *Nanoscale*, 2021, **13**(43), 17989–18009.

3 S. N. F. M. Nasir, H. Ullah, M. Ebadi, A. A. Tahir, J. S. Sagu and M. A. Mat Teridi, New insights into Se/$BiVO_4$ heterostructure for photoelectrochemical water splitting: a combined experimental and DFT study, *J. Phys. Chem. C*, 2017, **121**(11), 6218–6228.

4 B. Jin, Y. Cho, C. Park, J. Jeong, S. Kim, J. Jin, W. Kim, L. Wang, S. Lu, S. Zhang and S. H. Oh, A two-photon tandem black phosphorus quantum dot-sensitized $BiVO_4$ photoanode for solar water splitting, *Energy Environ. Sci.*, 2022, **15**(2), 672–679.

5 P. Yang, H. Shi, H. Wu, D. Yu, L. Huang, Y. Wu, X. Gong, P. Xiao and Y. Zhang, Manipulating the surface states of $BiVO_4$ through electrochemical reduction for enhanced PEC water oxidation, *Nanoscale*, 2023, **15**(9), 4536–4545.

6 L. Xia, J. Li, J. Bai, L. Li, Q. Zeng, Q. Xu and B. Zhou, Preparation of a $BiVO_4$ nanoporous photoanode based on peroxovanadate reduction and conversion for efficient photoelectrochemical performance, *Nanoscale*, 2018, **10**(6), 2848–2855.

7 Q. Yi, H. Wang and J. M. Lee, BiVO4—Based Photoelectrochemical Water Splitting, *ChemElectroChem*, 2025, **12**(4), e202400600.

8 H. L. Tan, R. Amal and Y. H. Ng, Alternative strategies in improving the photocatalytic and photoelectrochemical activities of visible light-driven $BiVO_4$: a review, *J. Mater. Chem. A*, 2017, **5**(32), 16498–16521.

9 J. Zhang, K. Chen, Y. Bai, L. Wang, J. Huang, H. She and Q. Wang, An MgO passivation layer and hydrotalcite derived spinel Co_2AlO_4 synergically promote photoelectrochemical water oxidation conducted using $BiVO_4$-based photoanodes, *Nanoscale*, 2024, **16**(20), 10038–10047.

10 H. Ullah, A. A. Tahir and T. K. Mallick, Structural and electronic properties of oxygen defective and Se-doped p-type $BiVO_4$ (001) thin film for the applications of photocatalysis, *Appl. Catal., B*, 2018, **224**, 895–903.

11 S. K. Cho, H. S. Park, H. C. Lee, K. M. Nam and A. J. Bard, Metal doping of $BiVO_4$ by composite electrodeposition with improved photoelectrochemical water oxidation, *J. Phys. Chem. C*, 2013, **117**(44), 23048–23056.

12 S. K. Pilli, T. E. Furtak, L. D. Brown, T. G. Deutsch, J. A. Turner and A. M. Herring, Cobalt-phosphate (Co-Pi) catalyst modified Mo-doped $BiVO_4$ photoelectrodes for solar water oxidation, *Energy Environ. Sci.*, 2011, **4**(12), 5028–5034.

13 X. Zhang, Y. Zhang, X. Quan and S. Chen, Preparation of Ag doped $BiVO_4$ film and its enhanced photoelectrocatalytic (PEC) ability of phenol degradation under visible light, *J. Hazard. Mater.*, 2009, **167**(1–3), 911–914.

14 C. Yin, S. Zhu, Z. Chen, W. Zhang, J. Gu and D. Zhang, One step fabrication of C-doped $BiVO_4$ with hierarchical structures for a high-performance photocatalyst under visible light irradiation, *J. Mater. Chem. A*, 2013, **1**(29), 8367–8378.

15 S. Obregón and G. Colón, Heterostructured Er^{3+} doped $BiVO_4$ with exceptional photocatalytic performance by cooperative electronic and luminescence sensitization mechanism, *Appl. Catal., B*, 2014, **158**, 242–249.

16 M. Wang, Q. Liu, Y. Che, L. Zhang and D. Zhang, Characterization and photocatalytic properties of N-doped $BiVO_4$ synthesized via a sol–gel method, *J. Alloys Compd.*, 2013, **548**, 70–76.

17 G. Tan, L. Zhang, H. Ren, J. Huang, W. Yang and A. Xia, Microwave hydrothermal synthesis of N-doped $BiVO_4$ nanoplates with exposed (040) facets and enhanced visible-light photocatalytic properties, *Ceram. Int.*, 2014, **40**(7), 9541–9547.

18 W. J. Jo, J. W. Jang, K. J. Kong, H. J. Kang, J. Y. Kim, H. Jun, K. P. Parmar and J. S. Lee, Phosphate doping into monoclinic $BiVO_4$ for enhanced photoelectrochemical water oxidation activity, *Angew. Chem., Int. Ed.*, 2012, **51**(13), 3147.

19 X. Zhao, J. Hu, B. Wu, A. Banerjee, S. Chakraborty, J. Feng, Z. Zhao, S. Chen, R. Ahuja, T. C. Sum and Z. Chen, Simultaneous enhancement in charge separation and onset potential for water oxidation in a $BiVO_4$ photoanode by W–Ti codoping, *J. Mater. Chem. A*, 2018, **6**(35), 16965–16974.

20 T. Iqbal, M. T. Qureshi, R. Shahzad, S. Afsheen, S. Kausar, G. Yunus, M. S. Mansha, L. Aamir, R. M. Munir, H. A. El-Serehy and M. Y. Khan, Synergistic impacts of novel tantalum doping in $BiVO_4$ for effective photocatalytic applications, antimicrobial activity, and antioxidant aspect, *Inorg. Chem. Commun.*, 2024, **170**, 113365.

21 K. Lai, Y. Zhu, J. Lu, Y. Dai and B. Huang, Synergistic effects of codopants on photocatalytic O_2 evolution in $BiVO_4$, *Solid State Sci.*, 2013, **24**, 79–84.

22 S. Lardhi, L. Cavallo and M. Harb, Significant impact of exposed facets on the BiVO4 material performance for photocatalytic water splitting reactions, *J. Phys. Chem. Lett.*, 2020, **11**(14), 5497–5503.

23 X. Li, Y. Zhang, Z. Fang, X. Feng, Y. Xu and H. Li, Halogen Atom (Cl, Br, and I) Doping Effects on the Electronic Character and OER Performance of $BiVO_4$ as a Photoanode Nanomaterial for Solar Water Splitting: A Theoretical Study, *Langmuir*, 2025, **41**(21), 13028–13040.

24 A. Massaro, A. Pecoraro, S. Hernandez, G. Talarico, A. B. Munoz-Garcia and M. Pavone, Oxygen evolution reaction at the Mo/W-doped bismuth vanadate surface: Assessing the dopant role by DFT calculations, *Mol. Catal.*, 2022, **517**, 112036.
25 W. Yao, H. Iwai and J. Ye, Effects of molybdenum substitution on the photocatalytic behavior of BiVO 4, *Dalton Trans.*, 2008, **11**, 1426–1430.
26 W. Guo, T. L. Ward, C. Porter and A. K. Datye, Phase content and particle morphology of Bi–Mo–V–O powders produced by aerosol pyrolysis, *Mater. Res. Bull.*, 2005, **40**(8), 1371–1387.
27 K. Ding, B. Chen, Z. Fang, Y. Zhang and Z. Chen, Why the photocatalytic activity of Mo-doped BiVO 4 is enhanced: a comprehensive density functional study, *Phys. Chem. Chem. Phys.*, 2014, **16**(26), 13465–13476.
28 G. Kresse and J. Furthmüller, Efficient iterative schemes for ab initio total-energy calculations using a plane-wave basis set, *Phys. Rev. B:Condens. Matter Mater. Phys.*, 1996, **54**(16), 11169.
29 J. P. Perdew, K. Burke and M. Ernzerhof, Generalized gradient approximation made simple, *Phys. Rev. Lett.*, 1996, **77**(18), 3865.
30 P. E. Blöchl, Projector augmented-wave method, *Phys. Rev. B:Condens. Matter Mater. Phys.*, 1994, **50**(24), 17953.
31 A. D. Becke, A new mixing of Hartree-Fock and local density-functional theories, *J. Chem. Phys.*, 1993, **98**(2), 1372–1377.
32 V. I. Anisimov and O. Gunnarsson, Density-functional calculation of effective Coulomb interactions in metals, *Phys. Rev. B:Condens. Matter Mater. Phys.*, 1991, **43**(10), 7570.
33 B. Cheng, H. Lou, Z. Zeng, Y. Liu and Q. Zeng, Structural phase transition in BiVO4 nanosheets under high pressure, *J. Phys. Chem. C*, 2024, **128**(29), 12267–12273.
34 A. W. Sleight, H. Y. Chen, A. Ferretti and D. E. Cox, Crystal growth and structure of BiVO4, *Mater. Res. Bull.*, 1979, **14**(12), 1571–1581.
35 Z. Zhao, Z. Li and Z. Zou, Structure and energetics of low-index stoichiometric monoclinic clinobisvanite BiVO 4 surfaces, *RSC Adv.*, 2011, **1**(5), 874–883.
36 W. J. Yin, S. H. Wei, M. M. Al-Jassim, J. Turner and Y. Yan, Doping properties of monoclinic $BiVO_4$ studied by first-principles density-functional theory, *Phys. Rev. B:Condens. Matter Mater. Phys.*, 2011, **83**(15), 155102.
37 K. Y. Yoon, J. Park, H. Lee, J. H. Seo, M. J. Kwak, J. H. Lee and J. H. Jang, Unveiling the role of the Ti dopant and viable Si doping of hematite for practically efficient solar water splitting, *ACS Catal.*, 2022, **12**(9), 5112–5122.
38 S. Chaule, J. Kang, B. G. Ghule, H. Kim and J. H. Jang, An Approach to enhance PEC water splitting performance through Al: Ti codoping in hematite (α-Fe2O3) photoanode: the effect of Al3+ as a Codopant, *ACS Mater. Lett.*, 2024, **6**(7), 2897–2904.
39 B. G. Ghule and J. H. Jang, Determining the Effect of Cation (Ti/Zr) Doping in Bismuth Oxide for Electrochemical CO_2 Reduction to Formic Acid: A DFT Study, *Energy Fuels*, 2023, **37**(23), 18009–18018.
40 J. Wang, J. Bai, Y. Zhang, L. Li, C. Zhou, T. Zhou, J. Li, H. Zhu and B. Zhou, Unconventional substitution for $BiVO_4$ to enhance photoelectrocatalytic performance by accelerating polaron hopping, *ACS Appl. Mater. Interfaces*, 2023, **15**(11), 14359–14368.
41 Z. Zhao, W. Luo, Z. Li and Z. Zou, Density functional theory study of doping effects in monoclinic clinobisvanite $BiVO_4$, *Phys. Lett. A*, 2010, **374**(48), 4919–4927.
42 H. P. Sarker, P. M. Rao and M. N. Huda, Niobium doping in $BiVO_4$: interplay between effective mass, stability, and pressure, *ChemPhysChem*, 2019, **20**(5), 773–784.
43 S. S. Kalanur, Y. J. Lee, H. Seo and B. G. Pollet, Enhanced photoactivity towards bismuth vanadate water splitting through tantalum doping: An experimental and density functional theory study, *J. Colloid Interface Sci.*, 2023, **650**, 94–104.
44 K. Okuno, H. Kato, J. J. M. Vequizo, A. Yamakata, H. Kobayashi, M. Kobayashi and M. Kakihana, Expansion of the photoresponse window of a $BiVO_4$ photocatalyst by doping with chromium(VI), *RSC Adv.*, 2018, **8**(67), 38140–38145.
45 S. Zhao, C. Jia, X. Shen, R. Li, L. Oldham, B. Moss, B. Tam, S. Pike, N. Harrison, E. Ahmad and A. Kafizas, The aerosol-assisted chemical vapour deposition of Mo-doped BiVO 4 photoanodes for solar water splitting: an experimental and computational study, *J. Mater. Chem. A*, 2024, **12**(39), 26645–26666.
46 N. T. K. Huyen, T. D. Pham, N. T. D. Cam, P. Van Quan, N. Van Noi, N. T. Hanh, M. H. T. Tung and V. D. Dao, Fabrication of titanium doped BiVO4 as a novel visible light driven photocatalyst for degradation of residual tetracycline pollutant, *Ceram. Int.*, 2021, **47**(24), 34253–34259.
47 S. Gofurov, D. Ide, L. G. Oktariza, M. M. Islam, S. Ikeda and T. Sakurai, Enhanced photoelectrochemical performance of Zr-doped BiVO4 photoanode deposited by co-sputtering, *Thin Solid Films*, 2025, **819**, 140665.
48 R. Liu, J. Ren, D. Zhao, J. Ning, Z. Zhang, Y. Wang, Y. Zhong, C. Zheng and Y. Hu, Band-gap engineering of porous BiVO 4 nanoshuttles by Fe and Mo co-doping for efficient photocatalytic water oxidation, *Inorg. Chem. Front.*, 2017, **4**(12), 2045–2054.
49 K. P. S. Parmar, H. J. Kang, A. Bist, P. Dua, J. S. Jang and J. S. Lee, Photocatalytic and photoelectrochemical water oxidation over metal–doped monoclinic BiVO4 photoanodes, *ChemSusChem*, 2012, **5**(10), 1926–1934.
50 L. L. Nascimento, R. A. Souza, P. H. H. Nunes, J. F. Costa, I. A. Ricardo, E. M. Oliveira, K. Krambrock, C. Wang and A. O. T. Patrocinio, Photoreforming of real biomass-derived waste streams using Nb-doped BiVO 4 photoanodes for sustainable hydrogen production, *RSC Sustainability*, 2025, **3**(10), 4504–4513.
51 S. S. Kalanur, Y. J. Lee, H. Seo and B. G. Pollet, Enhanced photoactivity towards bismuth vanadate water splitting through tantalum doping: An experimental and density functional theory study, *J. Colloid Interface Sci.*, 2023, **650**, 94–104.

52 Y. Lu, Y. Yang, X. Fan, Y. Li, D. Zhou, B. Cai, L. Wang, K. Fan and K. Zhang, Boosting charge transport in $BiVO_4$ photoanode for solar water oxidation, *Adv. Mater.*, 2022, **34**(8), 2108178.

53 J. Kang, B. G. Ghule, S. G. Gyeong, S. J. Ha and J. H. Jang, Alleviating charge recombination caused by unfavorable interaction of P and Sn in hematite for photoelectrochemical water oxidation, *ACS Catal.*, 2024, **14**(13), 10355–10364.

54 J. Greeley and J. K. Nørskov, Combinatorial density functional theory-based screening of surface alloys for the oxygen reduction reaction, *J. Phys. Chem. C*, 2009, **113**(12), 4932–4939.

55 X. Zhao, J. Hu, B. Wu, A. Banerjee, S. Chakraborty, J. Feng, Z. Zhao, S. Chen, R. Ahuja, T. C. Sum and Z. Chen, Simultaneous enhancement in charge separation and onset potential for water oxidation in a BiVO 4 photoanode by W–Ti codoping, *J. Mater. Chem. A*, 2018, **6**(35), 16965–16974.

56 T. Zhang, M. Chen, X. Zhu and P. Lin, A novel Ti-doped BiVO4 photoanode with NiFeOx cocatalyst for fast charge transfer towards enhanced photoelectrochemical water oxidation, *Int. J. Hydrogen Energy*, 2025, **107**, 469–477.

57 E. Fabbri, A. Habereder, K. Waltar, R. Kötz and T. J. Schmidt, Developments and perspectives of oxide-based catalysts for the oxygen evolution reaction, *Catal. Sci. Technol.*, 2014, **4**(11), 3800–3821.

58 M. G. Mavros, T. Tsuchimochi, T. Kowalczyk, A. McIsaac, L. P. Wang and T. V. Voorhis, What can density functional theory tell us about artificial catalytic water splitting?, *Inorg. Chem.*, 2014, **53**(13), 6386–6397.

59 H. Adamu, Z. H. Yamani and M. Qamar, Modulation to favorable surface adsorption energy for oxygen evolution reaction intermediates over carbon-tunable alloys towards sustainable hydrogen production, *Mater. Renew. Sustain. Energy*, 2022, **11**(3), 169–213.

60 K. Ding, L. Wen, L. Xu, H. Wu, Y. Ye and Y. Zhang, Predicting the electronic and optical properties of IB metals doped monoclinic BiVO4: First-principles calculations, *Int. J. Quantum Chem.*, 2016, **116**(5), 388–395.

61 H. L. Tan, R. Amal and Y. H. Ng, Alternative strategies in improving the photocatalytic and photoelectrochemical activities of visible light-driven $BiVO_4$: a review, *J. Mater. Chem. A*, 2017, **5**(32), 16498–16521.

62 Y. Liang, T. Tsubota, L. P. Mooij and R. van de Krol, Highly improved quantum efficiencies for thin film BiVO4 photoanodes, *J. Phys. Chem. C*, 2011, **115**(35), 17594–17598.

63 F. F. Abdi and R. Van De Krol, Nature and light dependence of bulk recombination in Co-Pi-catalyzed BiVO4 photoanodes, *J. Phys. Chem. C*, 2012, **116**(17), 9398–9404.

64 F. F. Abdi, T. J. Savenije, M. M. May, B. Dam and R. Van De Krol, The origin of slow carrier transport in $BiVO_4$ thin film photoanodes: a time-resolved microwave conductivity study, *J. Phys. Chem. Lett.*, 2013, **4**(16), 2752–2757.

65 H. Zheng, S. Ling, B. Kong, T. Zeng, S. Jiang and W. Wang, Donor and Acceptor Characteristics of Group IV and VII Doped BiNbO4: A Hybrid Density Functional Investigation, *Langmuir*, 2025, **41**(38), 26149–26165, DOI: 10.1021/acs.langmuir.5c02942.

66 I. Abdellaoui, M. M. Islam, M. Remeika, S. Kanno, R. Okamoto, K. Tajima, S. A. Pawar, Y. H. Ng, C. Budich, T. Maeda and T. Wada, Mechanism of incorporation of zirconium into $BiVO_4$ visible-light photocatalyst, *J. Phys. Chem. C*, 2021, **125**(6), 3320–3326.

67 H. P. Sarker, P. M. Rao and M. N. Huda, Niobium doping in $BiVO_4$: interplay between effective mass, stability, and pressure, *ChemPhysChem*, 2019, **20**(5), 773–784.

68 Y. Jia, Z. Wang, Y. Ma, J. Liu, W. Shi, Y. Lin, X. Hu and K. Zhang, Boosting interfacial charge migration of TiO_2/$BiVO_4$ photoanode by W doping for photoelectrochemical water splitting, *Electrochim. Acta*, 2019, **300**, 138–144.